Iron sites in radiation-damaged allanite-(Ce): the effects of thermally induced oxidation and structural reorganization

Claudia Eva Reissner [1] ⬤ · Michael Reissner [2] · Daniel Kern [2] · Herbert Pöllmann [1] · Tobias Beirau [1]

Abstract

Radiation-damaged allanite-(Ce) starts to recrystallize at an annealing temperature below 700 K. At the same temperature $Fe^{2+} \rightarrow Fe^{3+}$ oxidation, as well as dehydration occurs. Three radiation-damaged samples (S74 20414: 0.55 wt% ThO_2, LB-1: 1.18 wt% ThO_2, R1: 1.59 wt% ThO_2) as well as one crystalline sample (RS221) were investigated using ^{57}Fe Mössbauer spectroscopy after step-wise annealing. Additionally, the three damaged samples were investigated by in-situ mass spectrometry, analysing the escaping gases during thermal treatment showing the dehydration process. ^{57}Fe Mössbauer spectroscopy revealed not only a general $Fe^{2+} \rightarrow Fe^{3+}$ oxidation, it also showed that this process is not fully completed after annealing at 1000 K in sample LB-1 which is the sample showing the fastest and strongest recrystallization. The crystalline sample also still incorporated Fe^{2+} as well as Fe^{3+} after annealing at 1000 K. In addition, a preferred occupation of iron at the position M3 was identified in the crystalline sample which did not occur in the pristine radiation-damaged samples (M1/M3 site distribution: RS221: 17/83, pristine samples R1: 49/51, LB-1: 60/40, S74 20414: 52/48). After annealing at 1000 K sample LB-1 showed a similar distribution as the crystalline sample with a M1/M3 distribution of 15/85. It is therefore proposed that the process of amorphization through α-decay damage changes the distribution of iron atoms on its possible crystallographic sites, and that this process is reversible through thermal annealing.

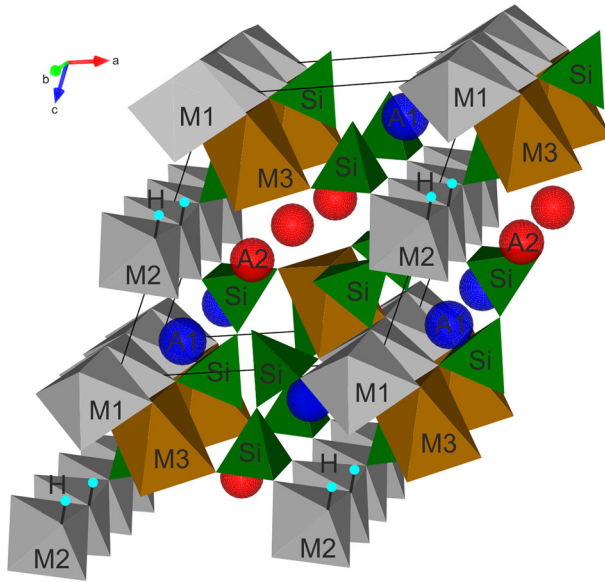**Keywords** Allanite · Radiation-damage · Mössbauer spectroscopy · Iron oxidation

✉ Claudia Eva Reissner
claudia.reissner@geo.uni-halle.de

Extended author information available on the last page of the article

Fig. 1 Schematic presentation of the ideal allanite-(Ce) structure visualised using the software Vesta. H-atoms have been added after Fig. 2 in [5]

1 Introduction

The mineral allanite can naturally incorporate up to 5 wt% ThO_2 and is an interesting model material to study long-term radiation damage effects. It crystallizes in a monoclinic structure ($P2_1/m$), with the ideal formula $^{A1}(Ca)^{A2}(REE)^{M1,M2}(Al)_2{}^{M3}(Fe^{2+})(Si_2O_7)(SiO_4)O(OH)$ [1–3] and belongs to the epidote supergroup. If the main REE (rare earth element) content is Ce it is denoted as allanite-(Ce) with the ideal formula $Ca(Ce,La,Ca)(Fe^{2+},Fe^{3+})(Al,Fe^{3+})Al(Si_2O_7)(SiO_4)O(OH)$ [1, 4]. Its structure is composed of two edge-sharing octahedra chains (M-positions) which are linked by SiO_4 and Si_2O_7 groups (Fig. 1) [6]. The octahedral and Si sites form polyhedral positions (A positions) which can incorporate Ca, Mn, and Na on the A1 position and on the A2 position lanthanides, as well as actinides such as U and Th or other cations (e.g. Sr, Pb, and Cd). Iron can be incorporated as Fe^{2+} or Fe^{3+} on the M1 and M3 sites. The M2 site mostly hosts Al [4]. A proton is attached to the O10 atom forming structural OH^- groups [5, 6].

The incorporation of actinides leads to alpha-decay events which causes structural amorphization (metamictization) over geological time. During such an event an α-particle ($^4_2He^{2+}$ nucleus) and a heavy recoil nucleus are generated [7]. Along its trajectory of ~15–22 μm the α-particle displaces several hundreds of atoms due to its comparably high energies (~4.5–5.8 MeV for actinides). Even though the recoil nucleus has lower kinetic energies (~70–100 keV) and a shorter trajectory of only ~30–40 nm its much higher weight leads to a displacement of several thousand atoms by elastic collisions [8].

Exposing to higher temperatures leads to recrystallization and thus to structural recovery. However, such a thermal treatment may also lead to further processes in the mineral (i.e. in the case of allanite: iron-oxidation and dehydration). It has been proposed that structural OH^- groups act as a catalyst in this recrystallization process [9–11].

Table 1 Investigated radiation-damaged samples and their age, ThO_2 content and calculated maximum α-dose

Sample	Age	ThO_2 concentration	Calculated dose
	Ma	wt% (from [11])	[α-decay/g]
S74 20,414	923 ± 8 [12]	0.55	3.5×10^{18}
LB-1	1520 [13]	1.18	2.0×10^{19}
R1	243.5 ± 2.1 [14, 15]	1.59	2.6×10^{18}

In this study, the oxidation of iron during thermal treatment as well as the changes in site occupation are studied with ^{57}Fe Mössbauer spectroscopy. Additionally, in-situ mass spectrometry measurements allowed us to follow the dehydration process.

2 Experimental

2.1 Allanite-(Ce) samples

Three allanite-(Ce) samples with varying ThO_2 content from different locations were studied. All samples were black to black-brown, opaque and have a vitreous luster. A detailed sample characterization can be found in [11].
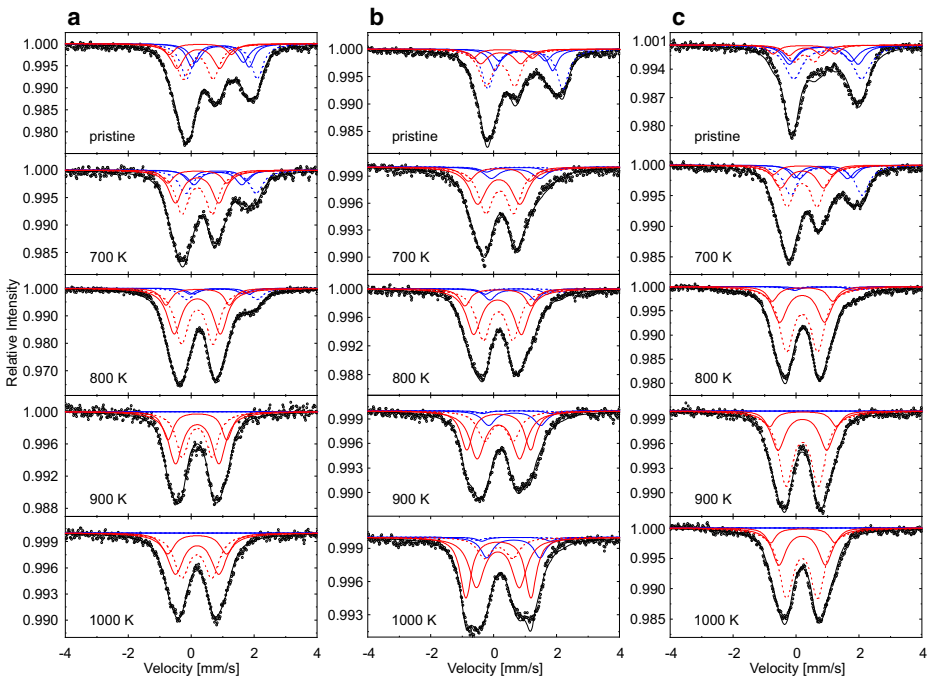
Fig. 2 ^{57}Fe Mössbauer spectra of samples (**a**) R1, (**b**) LB-1, and (**c**) S74 20414 for different annealing temperatures. Open circles denote the measured points, black line the calculated spectrum, blue subspectra are for Fe^{2+}, red subspectra for Fe^{3+}. Full lines denote M3 and dashed lines M1 sites. Hyperfine parameter for all spectra can be found in Table 4
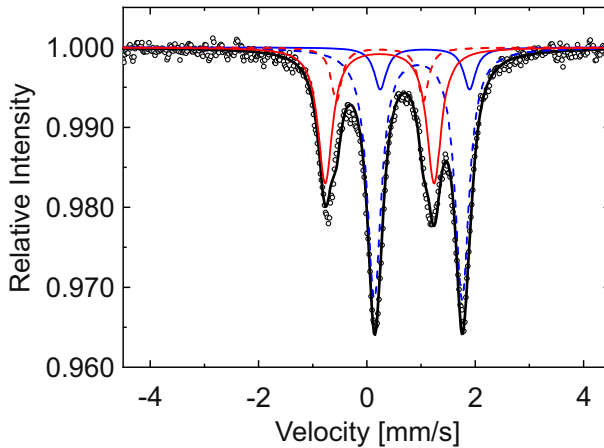
Fig. 3 ^{57}Fe Mössbauer spectrum of the crystalline reference sample RS221 without thermal treatment (pristine sample). Open circles denote the measured points, black line the calculated spectrum, blue subspectra are for Fe^{2+}, red subspectra for Fe^{3+}. Full lines denote M3 and dashed lines M1 sites. Hyperfine parameter can be found in Table 5

Sample S74 20,414, with a ThO$_2$ content of 0.55 wt% (see Table 1) was collected from the Hitterö Island in Norway. An age of 923 ± 8 Ma was obtained through U-Pb-Th dating on xenotimes in the surrounding pegmatitic rocks by Hetherington et al. [12].

Sample LB-1 with a ThO$_2$ content of 1.18 wt% (see Table 1) was collected from Holmtjärn in Sweden. An age of 1520 Ma was obtained through U-Pb-Th dating on surrounding rocks in the area by Welin & Blomqvist [13].

Sample R1, with a ThO$_2$ content of 1.59 wt% (see Table 1) was collected from the Savvushka area in the Altai Massif in the Russian Federation. An age of 243.5 ± 2.1 Ma was obtained using Rb-Sr isochrones on zircons from the northern Altai Mountains by Vladimirov et al. [14] and a similar age of 244 ± 1.1 Ma by ^{40}Ar/^{39}Ar dating on biotite in the same area by Gavryushkina et al. [15].

Table 2 Fe^{2+}/Fe^{3+} ratio of samples S74 20414, LB-1, R1 and the crystalline reference RS221 as measured by ^{57}Fe Mössbauer spectroscopy

Annealing temperature [K]		Pristine (300)	500	600	700	800	900	1000
S74 20,414	Fe^{2+} [%]	73 ± 2	81 ± 2	71 ± 2	42 ± 2	6 ± 2	0	0
	Fe^{3+} [%]	27 ± 2	19 ± 2	29 ± 2	58 ± 2	94 ± 2	100	100
	Fe^{2+}/Fe^{3+}	2.68	4.28	2.51	0.74	0.07	0.00	0.00
LB-1	Fe^{2+} [%]	53 ± 2	42 ± 2	53 ± 2	17 ± 2	13 ± 2	14 ± 2	16 ± 2
	Fe^{3+} [%]	47 ± 2	58 ± 2	47 ± 2	83 ± 2	87 ± 2	86 ± 2	84 ± 2
	Fe^{2+}/Fe^{3+}	1.17	0.71	1.15	0.20	0.14	0.18	0.19
R1	Fe^{2+} [%]	52 ± 2			35 ± 2	15 ± 2	0	0
	Fe^{3+} [%]	48 ± 2			65 ± 2	85 ± 2	100	100
	Fe^{2+}/Fe^{3+}	1.06			0.55	0.18	0	0
RS221	Fe^{2+} [%]	62 ± 2	61 ± 2	60 ± 2	61 ± 2	59 ± 2	53 ± 2	32 ± 2
	Fe^{3+} [%]	38 ± 2	39 ± 2	40 ± 2	39 ± 2	49 ± 2	47 ± 2	68 ± 2
	Fe^{2+}/Fe^{3+}	1.60	1.53	1.52	1.56	1.46	1.12	0.47
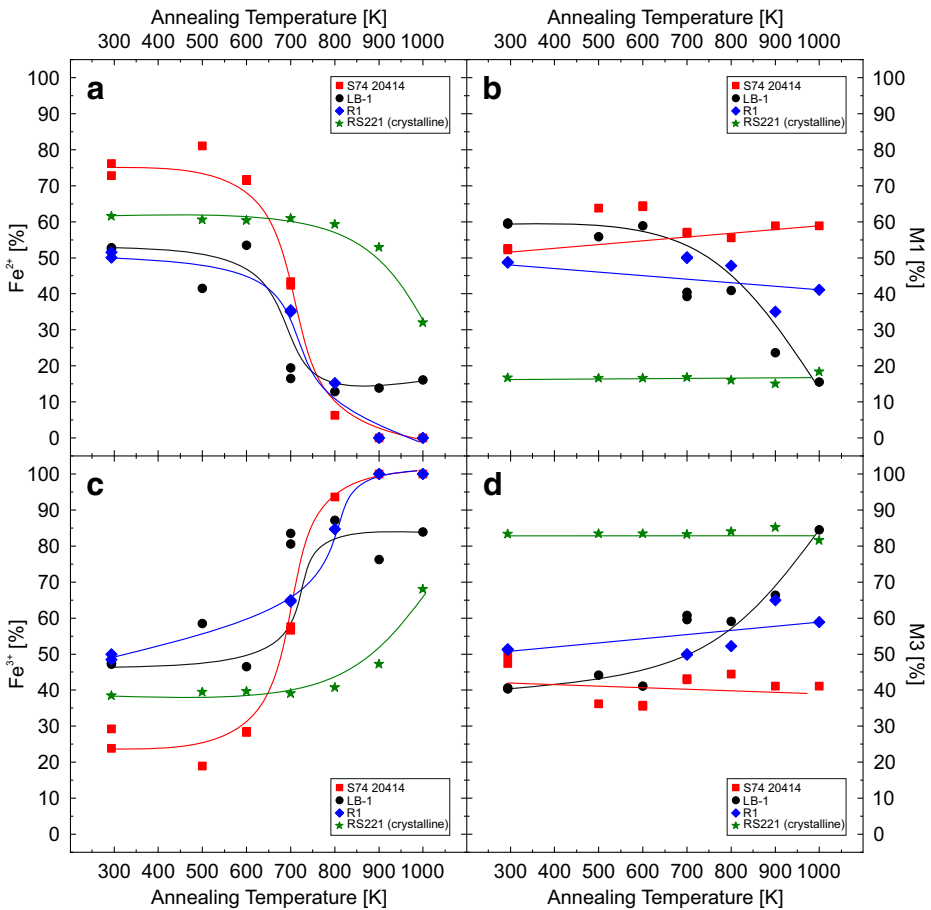
Fig. 4 (**a**) Fe^{2+} content, (**b**) amount of Fe-atoms on the M1 site, (**c**) Fe^{3+} content, and (**d**) amount of Fe-atoms on the M3 site are shown for samples S74 20414 (red squares), LB-1 (black circles), R1 (blue diamonds) and RS221 (green stars) as obtained by the fits (described in the text). Lines are only guides for the eyes

Assuming those ages for our specific samples a maximum life-time radiation dose (D) of 3.5×10^{18} α-decay/g, 2.0×10^{19} α-decay/g, and 2.6×10^{18} α-decay/g, for samples S74 20,414, LB-1, and R1, respectively, can be calculated using

$$D = 6 \frac{c_{Th} N_A}{M_{232} 10^6} \left(e^{\lambda_{232} t} - 1 \right)$$

with c_{Th} being the thorium concentration in ppm, N_A the Avogadro constant, M_{232} the atomic mass and λ_{232} the decay constant of the ^{232}Th isotope (from [16]), and t the integration time (after [17]).

According to X-ray diffraction sample LB-1 showed the fastest and strongest recrystallization of the three samples in the investigated temperature range [11].

Additionally, one crystalline sample RS221 from Nya Bastnäs, Sweden, was analyzed with ^{57}Fe Mössbauer spectroscopy as a reference.

Table 3 M1/M3 site distribution of Fe-atoms of samples S74 20414, LB-1, R1 and the crystalline reference RS221 as measured by [57]Fe Mössbauer spectroscopy

Annealing temperature [K]		Pristine (300)	500	600	700	800	900	1000
S74 20,414	M1 [%]	52 ± 1	64 ± 1	64 ± 1	57 ± 1	56 ± 1	59 ± 1	59 ± 1
	M3 [%]	48 ± 1	36 ± 1	36 ± 1	43 ± 1	44 ± 1	41 ± 1	41 ± 1
LB-1	M1 [%]	60 ± 1	56 ± 1	59 ± 1	40 ± 1	41 ± 1	24 ± 1	15 ± 1
	M3 [%]	40 ± 1	44 ± 1	41 ± 1	60 ± 1	59 ± 1	76 ± 1	85 ± 1
R1	M1 [%]	49 ± 1			50 ± 1	48 ± 1	35 ± 1	41 ± 1
	M3 [%]	51 ± 1			50 ± 1	52 ± 1	65 ± 1	59 ± 1
RS221	M1 [%]	17 ± 1	17 ± 1	17 ± 1	16 ± 1	16 ± 1	15 ± 1	18 ± 1
	M3 [%]	83 ± 1	83 ± 1	83 ± 1	84 ± 1	84 ± 1	85 ± 1	82 ± 1

2.2 Mössbauer spectroscopy

[57]Fe Mössbauer measurements were performed in standard transmission geometry in constant acceleration mode on powdered samples with a 19 mCi [57]Co**Rh** foil as a source. The full Hamiltonian was solved for the analysis and sample thickness was accounted for using the approximations by Mørup and Both [18]. All samples were step-wise annealed in air for an hour with a heating-up period of 30 min and cooled down to room temperature before measuring.

2.3 Thermal and evolved gas analyses

The powdered samples were heated in a corundum pan up to 1000 K with a heat rate of 10 K/min. The instrument was purged with synthetic air and the gases escaping during thermal treatment were analysed via mass spectrometry (MS) on a QMS 403D Aeolos Metzsch instrument.

3 Results and discussion

3.1 Mössbauer spectroscopy

The Mössbauer spectra of the pristine samples and after step-wise annealing are shown in Fig. 2. It was expected that four subspectra (according to Fe^{2+} and Fe^{3+} in the two crystallographic positions M1 and M3) are present adding up to the measured spectrum [6]. However, such a model did not fit well. Therefore, two subspectra were added to reach reasonable fitting results as seen in Fig. 2 and Table 4. This was also proposed by Malczewski & Grabias [19] who obtained a similar spectral shape for their highly irradiated sample ALL3. These additional spectra are explained as Fe^{2+} and Fe^{3+} at distorted M3 positions with different hyperfine parameters than for the ideal positions. The spectrum of the crystalline reference sample RS221 was well fit with only four spectra (Fig. 3, Table 5). All subspectra consist of doublets indicating that the iron is nonmagnetic. During annealing a $Fe^{2+} \rightarrow Fe^{3+}$ oxidation occurs, which is completed after annealing at 900 K in samples S74 20,414 and R1 leaving no remaining Fe^{2+} with Fe^{2+}/Fe^{3+} ratios of 73/27

Table 4 Hyperfine parameter of the spectra shown in Fig. 2

| T	Q1	CS1	G1	Int1	Q2	CS2	G2	Int2	Q3	CS3	G3	Int3	Q4	CS4	G4	Int4	Q5	CS5	G5	Int5	Q6	CS6	G6	Int6	r
K	mm/s	mm/s	mm/s	%	mm/s	mm/s	mm/s	%	mm/s	mm/s	mm/s	%	mm/s	mm/s	mm/s	%	mm/s	mm/s	mm/s	%	mm/s	mm/s	mm/s	%	
S74 20414																									
294	1.08	1.00	0.33	40	1.09	0.88	0.25	17	0.95	0.90	0.28	16	0.98	0.26	0.2	6	0.53	0.30	0.22	8	0.33	0.25	0.23	13	0.9868
500	1.12	0.96	0.27	50	0.9	0.87	0.22	16	0.74	0.90	0.25	15	0.93	0.22	0.22	3	0.68	0.21	0.29	2	0.47	0.20	0.28	14	0.9945
600	1.12	0.94	0.27	43	0.89	0.86	0.22	13	0.74	0.89	0.25	15	0.92	0.21	0.21	4	0.68	0.20	0.29	3	0.46	0.20	0.28	21	0.9957
700	1.13	0.99	0.29	25	0.89	0.91	0.23	9	0.74	0.91	0.26	10	0.94	0.22	0.22	6	0.70	0.21	0.29	19	0.48	0.21	0.28	32	0.9941
800	1.17	1.00	0.27	2	0.95	0.90	0.21	3	0.80	0.88	0.24	1	0.96	0.21	0.21	10	0.71	0.20	0.28	31	0.50	0.19	0.27	53	0.9976
900	1.20	1.03	0.27	0	0.99	0.93	0.21	0	0.84	0.91	0.24	0	1.07	0.22	0.20	10	0.77	0.20	0.27	31	0.52	0.20	0.28	59	0.9859
1000	1.20	1.03	0.27	0	0.99	0.93	0.21	0	0.84	0.91	0.24	0	1.02	0.22	0.20	10	0.74	0.20	0.27	31	0.50	0.19	0.27	59	0.9942
LB-1																									
294	1.19	1.01	0.22	30	0.92	0.96	0.19	14	0.74	0.92	0.22	9	0.94	0.29	0.19	6	0.63	0.23	0.25	12	0.46	0.21	0.25	29	0.9951
500	1.18	1.04	0.23	30	0.92	0.99	0.20	14	0.74	0.95	0.23	9	0.96	0.30	0.20	6	0.65	0.24	0.26	12	0.47	0.22	0.26	29	0.9953
600	1.19	1.04	0.23	21	0.94	0.99	0.20	11	0.75	0.95	0.23	10	0.97	0.30	0.20	8	0.65	0.23	0.25	16	0.47	0.22	0.25	35	0.9922
700	1.20	0.92	0.32	4	1.03	0.88	0.26	4	0.80	0.82	0.31	11	0.96	0.21	0.26	12	0.65	0.21	0.31	33	0.45	0.22	0.27	36	0.9952
800	1.28	0.86	0.20	2	0.98	0.71	0.18	3	0.72	0.60	0.22	7	1.05	0.14	0.21	11	0.76	0.13	0.29	38	0.48	0.14	0.27	38	0.9963
900	1.33	0.86	0.25	2	1.08	0.75	0.21	2	0.83	0.67	0.25	11	1.02	0.16	0.22	25	0.68	0.15	0.29	39	0.45	0.17	0.27	22	0.9939
1000	1.36	0.84	0.23	2	1.09	0.72	0.19	2	0.85	0.63	0.23	12	1.03	0.15	0.21	34	0.68	0.14	0.29	36	0.45	0.15	0.26	14	0.9925
R1																									
294	1.12	0.98	0.23	24	0.91	0.93	0.20	14	0.76	0.90	0.23	12	0.99	0.29	0.20	7	0.68	0.23	0.26	18	0.48	0.22	0.25	25	0.9972
700	1.13	0.98	0.28	19	0.95	0.91	0.21	7	0.79	0.90	0.24	10	0.98	0.22	0.20	8	0.73	0.20	0.27	25	0.50	0.21	0.25	31	0.9966
800	1.11	0.97	0.25	8	0.95	0.01	0.19	3	0.80	0.87	0.22	4	1.01	0.21	0.20	10	0.73	0.19	0.27	35	0.50	0.19	0.26	40	0.9983
900	0	0	0	0	0	0	0	0	0	0	0	0	0.94	0.20	0.20	19	0.69	0.19	0.27	46	0.48	0.19	0.24	35	0.9921
1000	0	0	0	0	0	0	0	0	0	0	0	0	0.94	0.19	0.25	18	0.69	0.19	0.30	41	0.48	0.18	0.29	41	0.9948

Qn denotes the quadrupole splitting $eQV_{zz}/4$, CSn the center shift relative to [57] **CoRh**, Gn the half width in mm/s Intn the relative intensity in % and r the correlation coefficient

Table 5 Hyperfine parameter for crystalline sample RS221 annealed at different temperatures

T	Fe²⁺ M3				Fe²⁺ M1				Fe³⁺ M3				Fe³⁺ M1				r
	Q1	CS1	G1	Int1	Q2	CS2	G2	Int2	Q3	CS3	G3	Int3	Q4	CS4	G4	Int4	
K	mm/s	mm/s	mm/s	%	mm/s	mm/s	mm/s	%	mm/s	mm/s	mm/s	%	mm/s	mm/s	mm/s	%	
298	0.81	0.95	0.16	54	0.82	1.07	0.14	8	1.01	0.24	0.16	30	0.8	0.24	0.12	9	0.9932
500	0.84	0.95	0.14	51	0.85	1.15	0.12	9	0.97	0.26	0.15	32	0.77	0.23	0.11	7	0.9891
600	0.82	0.94	0.12	51	0.84	1.12	0.11	9	0.97	0.24	0.14	32	0.77	0.21	0.11	8	0.9818
700	0.82	0.94	0.12	52	0.84	1.12	0.11	9	0.97	0.24	0.14	31	0.77	0.21	0.11	8	0.9572
800	0.82	0.94	0.14	51	0.87	1.14	0.12	9	0.99	0.26	0.15	33	0.78	0.22	0.11	7	0.9733
900	0.82	0.95	0.13	45	0.85	1.13	0.11	8	1.01	0.25	0.16	40	0.80	0.21	0.11	7	0.9678
1000	0.79	0.94	0.13	23	0.84	1.14	0.12	9	1.11	0.25	0.19	58	0.86	0.23	0.13	10	0.9790

Qn denotes the quadrupole splitting $eQV_{zz}/4$, CSn the center shift relative to ^{57} Co**Rh**, Gn the half width in mm/s Intn the relative intensity in % and r the correlation coefficient
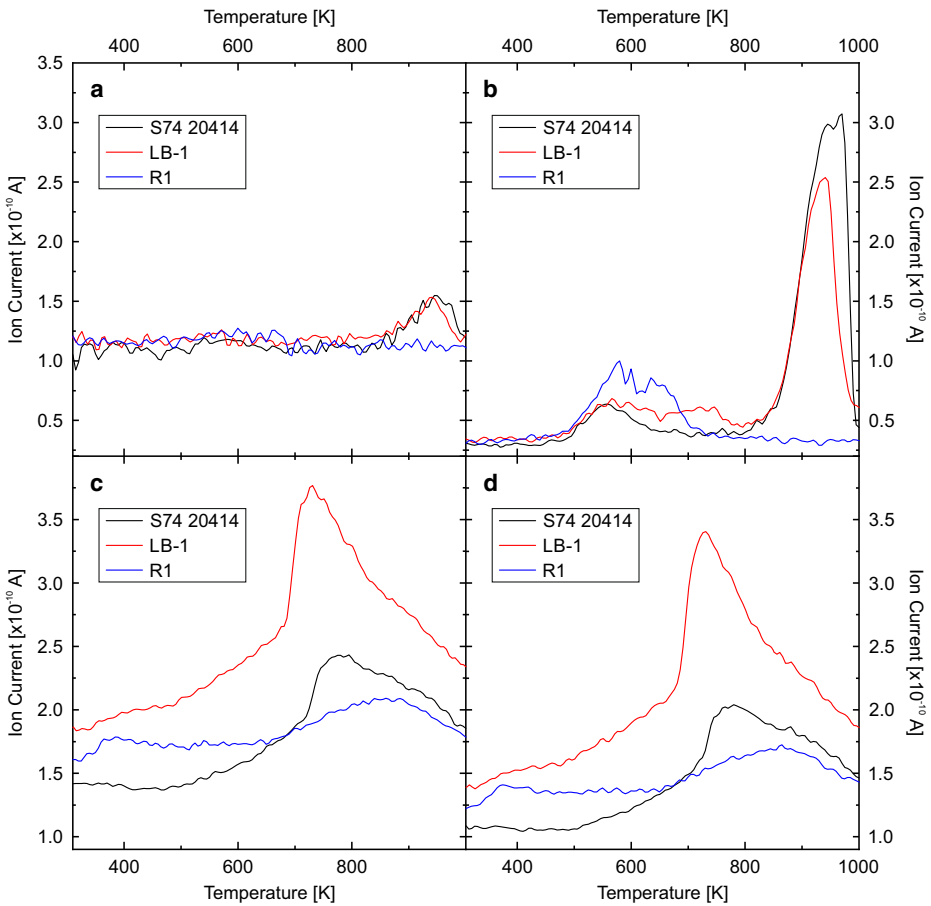
Fig. 5 Mass spectrometry measurements of the gas streams when heating samples S74 20414 (black), LB-1 (red) and R1 (blue), (**a**) Mass 12 (C), (**b**) Mass 44 (CO_2), (**c**) Mass 17 (OH) and (**d**) Mass 18 (H_2O)

and 52/48 in the pristine samples S74 20,414 and R1, respectively. Sample LB-1 however still showed 16% Fe^{2+} after annealing at 1000 K (Table 2, Fig. 4). The distribution of iron on the positions M1 and M3 is 52/48, 60/40, and 49/51 in the pristine samples S74 20,414, LB-1 and R1, respectively (Table 3, Fig. 4). The pristine crystalline sample showed an Fe^{2+}/Fe^{3+} ratio of 62/38 and a site distribution M1/M3 of 17/83. After annealing at 1000 K the Fe^{2+}/Fe^{3+} ratio changed to 32/68 but the site distribution M1/M3 stayed almost the same at 18/82. In differential calorimetric measurements an endothermic process can be seen starting just below 700 K [11], while at 700 K iron oxidation started according to ^{57}Fe Mössbauer spectroscopy (Table 2, Fig. 4a, c).

After annealing at 1000 K the site distribution of samples S74 20,414 and R1 showed a non-significant change to 59/41, 41/59 for M1/M3, respectively. However, in sample LB-1 a redistribution of iron atoms to the M3 site takes place leading to an M1/M3 ratio of 15/85 (Table 3, Fig. 4). This corresponds well with the preferred site for iron in the crystalline sample (RS221 M1/M3: 18/82).

3.2 Mass spectrometry

In sample S74 20,414 a loss of hydrogen can be seen starting at ~600 K (Fig. 5c, d). This behaviour is also visible in samples LB-1 and R1 (Fig. 5c, d), where the latter additionally shows a smaller peak at lower temperatures (maximum at ~400 K) which is most likely due to the loss of adhering water. The higher peak is attributed to the loss of structural H^+. Sample LB-1 showed the most hydrogen loss (see Fig. 5c, d).

Additionally, C and CO_2 was detected in the gas stream starting at temperatures of ~850 K in samples S74 20,414 and LB-1, with a smaller peak occuring already at temperatures of ~500–650 K for CO_2. In sample R1 only the earlier peak in CO_2 is visible and none in C (Fig. 5a, b). This is most likely due to the dissemination of calcite-microinclusions as mentioned by Papunen & Lindsjö [20].

4 Conclusion

Crystalline allanite-(Ce) showed an iron site distribution in two crystallographic positions with a preferred position M3 (M1/M3: 17/83) and an Fe^{2+}/Fe^{3+} ratio of 62/38. In the pristine radiation-damaged samples no preferred position was detected. However, during recrystallization this preferred distribution seems to be re-established as can be seen in sample LB-1 which showed an M1/M3 ratio of 15/85 after annealing at 1000 K. Additionally, this sample showed incomplete $Fe^{2+} \rightarrow Fe^{3+}$ oxidation after annealing at the same temperature. The same is true for the crystalline reference RS221 with an Fe^{2+}/Fe^{3+} ratio of 32/68 after annealing at 1000 K. Therefore, it is proposed that during radiation-damaged induced amorphization the iron atoms redistribute into a more evenly distribution of their possible positions. This process is likely reversed during thermally induced recrystallization. Additionally, the incomplete oxidation process in sample LB-1 (strongest recrystallization) as well as in the crystalline sample RS221, might be due to a lesser susceptibility of the Fe atoms in a crystalline surrounding to oxidation. Instead, the Fe^{2+} atoms in amorphized regions are oxidized first, which would explain the complete oxidation in samples S74 20,414 and R1, showing less structural reorganization than sample LB-1.

References

1. Armbruster, T., Bonazzi, P., Akasaka, M., Bermanec, V., Chopin, C., Gieré, R., Heuss-Assbichler, S., Liebscher, A., Menchetti, S., Pan, Y., Pasero, M.: Recommended nomenclature of epidote-group minerals. Eur. J. Mineral. **18**, 551–567 (2006)
2. Bonazzi, P., Holtstam, D., Bindi, L., Nysten, P., Capitani, G.C.: Multi-analytical approach to solve the puzzle of an allanite-subgroup mineral from Kesebol, Västra Götaland, Sweden. Am. Mineral. **94**, 121–134 (2009)
3. Mills, S.J., Hatert, F., Nickel, E.H., Ferraris, G.: The standardisation of mineral group hierarchies: application to recent nomenclature proposals. Eur. J. Mineral. **21**, 1073–1080 (2009)
4. Ercit, T.S.: The mess that is "allanite". Can. Mineral. **40**, 1411–1419 (2002)
5. Kartashov, P.M., Ferraris, G., Ivaldi, G., Sokolova, E., McCammon, C.A.: Ferriallanite-(Ce), $CaCeFe^{3+}AlFe^{2+}(SiO_4)(Si_2O_7)O(OH)$, a new member of the epidote group: description, X-ray and Mössbauer study. Can. Miner. **40**, 1641–1648 (2002)

6. Dollase, W.A.: Mössbauer spectra and iron distribution in the epidote-group minerals. Z. Kristallogr. **138**, 41–63 (1973)
7. Ewing, R.C., Meldrum, A., Wang, L.M., Wang, S.X.: Radiation-induced amorphization. Rev. Mineral. Geochem. **39**, 319–361 (2000)
8. Ewing, R.C.: Actinides and radiation effects: impact on the back-end of the nuclear fuel cycle. Mineral. Mag. **75**, 2359–2377 (2011)
9. Čobić, A., Bermanec, V., Tomašić, N.: The hydrothermal recrystallization of metamict allanite-(Ce). Can. Mineral. **48**, 513–521 (2010)
10. Zhang, M., Salje, E.K.H., Malcherek, T., Bismayer, U., Groat, L.A.: Dehydration of metamict titanite: an infrared spectroscopic study. Can. Mineral. **38**, 119–130 (2000)
11. Reissner, C.E., Bismayer, U., Kern, D., Reissner, M., Park, S., Zhang, J., Ewing, R.C., Shelyug, A., Navrotsky, A., Paulmann, C., Škoda, R., Groat, L.A., Pöllmann, H., Beirau, T.: Mechanical and structural properties of radiation-damaged allanite-(Ce) and the effects of thermal annealing. Phys. Chem. Mineral. **46**(10), 921–933 (2019)
12. Hetherington, C.J., Jercinovic, M.J., Williams, M.L., Mahan, K.: Understanding geological processes with xenotime: composition, chronology, and a protocol for electron probe microanalysis. Chem. Geol. **254**, 133–147 (2008)
13. Welin, E., Blomqvist, G.: Age measurements on radioactive minerals from Sweden. Geol. Foren. Stock. For. **86**, 33–50 (1964)
14. Vladimirov, A.G., Ponomareva, A.P., Shokalskii, S.P., Khalilov, V.A., Kostitsyn, Y.A., Ponomarchuk, V.A., Rudney, S.N., Vystavnoi, S.A., Kruk, N.N., Titov, A.V.: Late Paleozoic early Mesozoic granitoid magmatism in Altai. Geol. Geofiz. **38**, 715–729 (1997)
15. Gavryushkina, O.A., Travin, A.V., Kruk, N.N.: Duration of granitoid magmatism in peripheral parts of large igneous provinces (based on ^{40}Ar/^{39}Ar isotopic studies of Altai Permian-Triassic granitoids). Geodyn. Tectonophys. **8**, 1035–1047 (2017)
16. Firestone, R.B., Shirley, V.S.: Table of isotopes 2. Wiley, New York (1996)
17. Nasdala, L., Wenzel, M., Vavra, G., Irmer, G., Wenzel, T., Kober, B.: Metamictisation of natural zircon: accumulation versus thermal annealing of radioactivity-induced damage. Contrib. Mineral. Petrol. **141**, 125–144 (2001)
18. Mørup, S., Both, E.: Interpretation of Mössbauer spectra with broadened lines. Nucl. Inst. Methods. **124**, 445–448 (1975)
19. Malczewski, D., Grabias, A.: ^{57}Fe Mössbauer spectroscopy of radiation damaged Allanites. Acta Phys. Pol. A. **114**, 1683–1690 (2008)
20. Papunen, H., Lindsjö, O.: Apatite, monazite and allanite: three rare earth minerals from Korsnäs, Finland. Bul. Geol. Soc. Finl. **44**, 123–129 (1972)

Publisher's note   Springer Nature remains neutral with regard to jurisdictional claims in published maps and institutional affiliations.

Affiliations

Claudia Eva Reissner[1] · Michael Reissner[2] · Daniel Kern[2] · Herbert Pöllmann[1] · Tobias Beirau[1]

Michael Reissner
reissner@tuwien.ac.at

Daniel Kern
e1326150@student.tuwien.ac.at

Herbert Pöllmann
herbert.poellmann@geo.unihalle.de

Tobias Beirau
tobias.beirau@geo.uni-halle.de

[1]   Martin-Luther-University, Von-Seckendorff-Platz 3, Halle/Saale 06120, Germany

[2]   TU Wien, Wiedner Hauptstraße 8-10, 1040 Wien, Austria